Dual-band left-handed metamaterials fabricated by using tree-shaped fractal*

Xu He-Xiu(许河秀)[a)†], Wang Guang-Ming(王光明)[a)], Wang Jia-Fu(王甲富)[b)], and Yang Zi-Mu(杨自牧)[a)]

[a)] *Missile Institute, Air Force Engineering University, Xi'an* 710051, *China*

[b)] *College of Science, Air Force Engineering University, Xi'an* 710051, *China*

(Received 6 April 2012; revised manuscript received 11 June 2012)

A method of fabricating dual-band left-handed metematerials (LHMs) is investigated numerically and experimentally by single-sided tree-like fractals. The resulting structure features multiband magnetic resonances and two electric resonances. By appropriately adjusting the dimensions, two left-handed (LH) bands with simultaneous negative permittivity and permeability are engineered and are validated by full-wave eigenmode analysis and measurement as well in the microwave frequency range. To study the multi-resonant mechanism in depth, the LHM is analysed from three different perspectives of field distribution analysis, circuit model analysis, and geometrical parameters evaluation. The derived formulae are consistent with all simulated results and resulting electromagnetic phenomena, indicating the effectiveness of the established theory. The method provides an alternative to the design of multi-band LHM and has the advantage of not requiring two individual resonant particles and electrically continuous wires, which in turn facilitates planar design and considerably simplifies the fabrication.

Keywords: planar left-handed metamaterial, multi-band metamaterial, fractal, eigenmode

PACS: 41.20.Jb, 42.25.Bs, 73.20.Mf, 78.67.Pt **DOI:** 10.1088/1674-1056/21/12/124101

1. Introduction

Since the first experimental demonstration of negative refractive index of materials consisting of split ring resonators (SRRs) and rods,[1] left-handed (LH) metamaterials (LHMs) each with a periodic array of subwavelength particles exhibiting simultaneously negative permittivity ($\varepsilon_{\rm eff}$) and permeability ($\mu_{\rm eff}$) that do not occur in nature have received intense attention and explosively developed. Afterwards, a great variety of LHMs were proposed and experimentally studied to exhibit negative electric and magnetic response at the designed frequencies, such as S-shaped resonators,[2] Ω-shaped resonators,[3−5] labyrinth-based structure,[6] H-shaped[7] and cut wire[8] metallic pattern pairs, electric resonator pairs,[9] dendritic[10] and fishnet[11] structure, asymmetric H-shaped structure,[12] electric and magnetic resonators,[13,14] hexagonal SRRs with asymmetric defects,[15] ferrite combined with magnetic resonators,[16] spiral array,[17] metal-dielectric-metal sandwich structures in optical band,[18] and even three-dimensional broadband LHMs using cross-pairs.[19] Most recently, the authors even proposed an LHM with tri-band of negative refraction based on multi single split ring resonator pairs[20] and others also designed terahertz metamaterial absorber suitable for multifrequencies.[21] However, among them only a few LHMs have been reported to exhibit LH property over multiple frequency bands,[2,14−18] which should be a significant drawback and constraint to practical applications. Moreover, the rudimental idea of already emerged multiband (MB) LHMs is to combine a chain of LH unit cells or incorporating individual electric resonators and magnetic resonators with different geometrical dimensions, and to facilitate MB magnetic resonances in a broadband electric response, or MB electric resonances in a broadband magnetic response.

Fractal concept perturbed in electromagnetic (EM) theory has aroused the particular interest in science community due to the self-similarity and space-filling nature, for instance, the fractally perturbed metamaterial transmission lines were recently reported by Xu *et al.*[22,23] Up to now, only H-shaped fractal patterns have been widely used to design MB

*Project supported by the National Natural Science Foundation of China (Grant No. 60971118) and the Innovation Foundation for Postgraduate's Dissertation of Air Force Engineering University, China (Grant No. DY12101).

†Corresponding author. E-mail: hxxu20008@yahoo.cn

© 2012 Chinese Physical Society and IOP Publishing Ltd

electric[24] and magnetic[25] resonant metamaterials, terahertz photonic band gaps (PBG),[26] and most recently the MB LHMs.[27] Although MB LH behavior was engineered, further simplification of the complex bilayer fractal patterns is still required. Moreover, the limitation of H-shaped fractal makes the design of an alternative, improved, and a simplified fractal LHM that can be easily fabricated and theoretically characterized a pressing task. In this paper, we report on an innovative MB LHM fabricated using tree-shaped fractals numerically and experimentally for the first time. Quite different from the materials fabricated by the previous method, i.e., by combining a chain of different sized unit cells,[2,14] the present MB LHM possesses a coplanar structure without individual electric resonators and magnetic resonators, and furthermore the MB LH behaviour can be modulated. The operating frequency of the tree array may be extended at optical wavelengths in analogy to SRRs[28] provided that the magnetic properties can be realized, which is still in progress and deserves to be further investigated.

2. DNG Behaviour of the MB LHM

The second-order tree-shaped fractal used in this study is outlined in Fig. 1, which was initially used for an antenna design.[29] The construction law can be simply described as follows. Divide an initial line with length b into three equal segments, followed by drawing two lines each with a length of $b/3$ perpendicular to the initial line at the first and second cut-points, respectively. After this basic step, five equal segments are obtained and each of them is considered as a fresh line in the next step to form higher-order fractals by the same procedure. The iteration order (N), b, together with the line width w, horizontal gap $g_{\rm h}$, and vertical gap $g_{\rm v}$ which separates the six closed areas (C-shaped split ring resonators, in essence, C-SRRs) collectively determines the LHM cell. There is an asymmetry along its two orthogonal directions (y and z directions) within the plane of present cell, thus the complex conductor structure is anisotropic. However, here we restrict our characterization of the material to one of its principal axes. Therefore, there are only two scalar components permittivity and permeability relevant. To enhance the coupling and in turn obtain a strong electric resonance, the tree fractals are not directly applicable to the current LHM design. In this regard, a transformation is required, that is, rotating three segments outlined in the two black dashed at both ends by 90° in opposite directions. The coupling between neighbouring cells formed through the capacitive gap of a pair of horizontal wires is stronger than that obtained from cut wire.

The engineered strong coupling plus the inductive central pole facilitates a strong fundamental electric resonance at $\omega_{\rm e0}$ (Lorentz-type dispersion characteristic). Moreover, the plasma frequency $\omega_{\rm ep}$ (Drude-type dispersion) of the central vertical pole is still available and is unaffected by the electrical resonance. The analytical calculations suggest that $\varepsilon_{\rm eff}$ obeys the cut-wire response form,[30]

$$\varepsilon_{\rm eff}(\omega) = 1 - \frac{\omega_{\rm ep}^2 - \omega_{\rm e0}^2}{\omega^2 - \omega_{\rm e0}^2 + {\rm i}\gamma\omega}, \tag{1}$$

where γ is the damping factor. Despite this electric resonance, a further inspection indicates that the LHM structure exhibits at least one additional electric resonance, providing the negative permittivity. The speculation is subjected to being decomposed into two electric parts of the LHM cell shown in Fig. 1(b). The former one is analogous to the H-shaped metallic wire[7] associated with aforementioned electric response of cut wires, whereas the remaining one is a newly fashioned electric-field-coupled (ELC) resonator displaying a narrow band of negative permittivity in the vicinity of electric resonance.[13] Notice that the two decoupled parts related to electric response do not correspond to the original LHM cell because there are also magnetic parts constituting the cell. Different from its previous counterpart, the ELC resonator has interlaced side arms (poles) and thus is asymmetric along y axis. Moreover, the corresponding electric resonance is strongly affected by the coupling in the top-and-bottom region of two adjacent unit cells on the same side of board. Aside from these electrical behaviours, higher electric modes may be also expected to be formed through oscillation of linear current along vertical side poles and splits. Since these electric modes are less important from the point of view of LH behaviour and the effective medium concept, they are excluded from our discussion. We will concentrate on the study of first two electric resonances in the LHM design.

As to the magnetic behaviour, more than two magnetic resonances can be predicted from the multi C-SRRs (from C-SRR$_1$ to C-SRR$_6$), say, the funda-

mental magnetic resonance formed through the horizontal C-SRR$_1$ and C-SRR$_6$ in the up-and-down region of two adjacent cells and the second one realized through vertical C-SRRs in left-and-right region of the LHM cell. The structure asymmetry implies that even uniform sized C-SRRs at different positions may resonate with different magnetic responses. The frequency dependence of the effective permeability at the i-th magnetic resonance $\omega_{\rm m0}^{(i)}$ is suggested as an analog of Lorentz-type dispersion by introducing a correctional factor a_i

$$\mu_{\rm eff}(\omega) = 1 - a_i \frac{\omega_{\rm mp}^{(i)^2} - \omega_{\rm m0}^{(i)^2}}{\omega^2 - \omega_{\rm m0}^{(i)^2} + {\rm i}\gamma\omega}, \tag{2}$$

$$\omega_{\rm mp}^{(i)^2} = \omega_{\rm m0}^{(i)^2}/(1 - F_i), \tag{3}$$

where $\omega_{\rm mp}^{(i)}$ is the i-th magnetic plasma frequency, and F_i is the filling factor of the i-th resonator and its value is smaller than unity, namely, the area ratio between the interior ring and the total resonator.

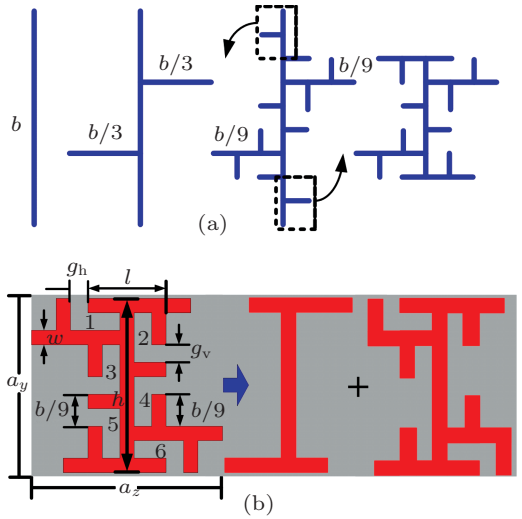


Fig. 1. (colour online) (a) Schematics of the formation of the proposed MTM unit cell based on tree-shaped fractal geometry and (b) the dimension illustration of the lattice constant and geometrical parameters, and structure decomposing.

For characterization, numerical simulation is carried out by using commercial full-wave finite-element-method (FEM) EM field solver Ansoft' High-Frequency Structure Simulator (HFSS). Figure 2 illustrates the simulation setup of the proposed LHM cell and the representation of the final fabricated LHM slab. The transverse EM (TEM) wave was incident along the z direction with the electric field polarized in the direction parallel to y axis and magnetic field parallel to x axis. The four boundaries of the LHM cell along the x and y directions are assigned as periodic boundary conditions (PBC) (master/slave in the Ansoft HFSS) to mimic infinite unit cells in the x–y plane. Two ports with a distance of more than $\lambda/8$ from the array at the open ends are assigned as Floquet ports (input or output ports) to avoid any high-order mode and the resulting phase lag can be eliminated by deembedding technique in HFSS, where λ is the free-space wavelength evaluated at the minimum frequency. A waveguide excitation of TE mode is assigned at the two ports to guarantee the environment of electric field along the y direction and the magnetic field along the x axis. This setup is a good approximation to the measurement environment in a waveguide which operates in its dominant TE10 mode. In the simulations, the metal material we used is copper with conductivity $\sigma = 5.8 \times 10^7$ S/m and thickness $t = 0.018$ mm, and the substrate is the microwave composite laminate with a dielectric constant of $\varepsilon_{\rm r} = 9.6$, a thickness of $h = 1$ mm, and a measured dielectric loss tangent $\tan\delta = 0.001$. Dimensions of the unit cell are $b = 8$ mm, $w = 0.4$ mm, and $g_{\rm v} = g_{\rm h} = 0.48$ mm. The periodicity (lattice constant) along the magnetic direction a_x and electric direction

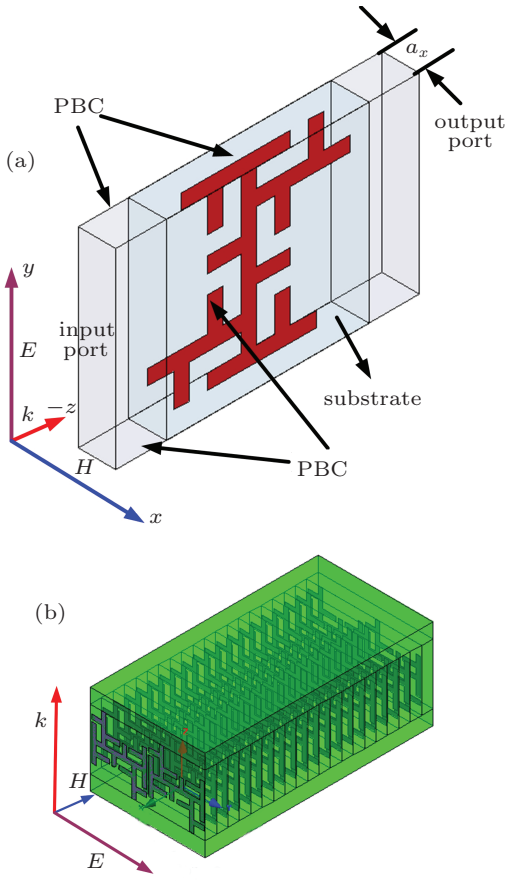


Fig. 2. (colour online) (a) Simulation setup of proposed tree-shaped LHM slab and (b) schematic plot of pattern array with an edge illumination by a plane wave.

a_y are 1 mm and 5.04 mm, respectively. The layer thickness a_z along the wave propagation direction is 5.33 mm.

Figure 3 depicts the simulated transmission spectra of the LHM cell by employing the simulation setup shown in Fig. 2 in conjunction with the effective μ_{eff}, ε_{eff}, and refractive index retrieved using the standard algorithm[31,32] in a broadband frequency range. The algorithm which is routinely appropriate to the artificial subwavelength metamaterial whose cell dimension is on the order of $\lambda_0/10$ or even smaller on the principle of averaging the local responding EM fields and current distributions has been used to demonstrate the dual-band negative refraction of LHMs by one of the authors,[14] where the λ_0 is the free-space wavelength at the operating frequency. Recently, it has been successfully extended to the double negative LHM whose cell dimension is comparable to λ_0.[33] It is important to notice that all these retrieved effective material parameters (EMPs) are conceptually not the characteristic material parameters defined in Ref. [34] because there exists always a difference in EM characteristic between its equivalence filled with effective medium and the composites in practice. Most recently, some researchers claimed that different signs of imaginary parts of μ_{eff} and ε_{eff} and the so-called antiresonances deviate from the basic condition of passivity and causality, and proposed even new analytic homogenization models to avoid these pitfalls by taking the magnetoelectric coupling into account.[35,36] However, the homogenization approach for artificial materials is still a long-standing and disputing issue and no more rigorous retrieval procedure to extract effective parameters from transmission and reflection coefficients has been reported up to now. In this circumstance, the authors do not address this issue and have some reservations on it. Despite these, the EMPs offer an important physical insight into the nature of the EM response of a composite such as the characterization of electric or magnetic resonances and negative refractive index.

The branches of real part of n and z are cautiously determined by using the standard algorithm. Consulting Fig. 3(a), two obvious transmission peaks occurring at 8.32 GHz and 10.2 GHz are observed. Two return loss valleys better than -10 dB are good except for a slight deterioration in the higher band, indicating that the LHM matches well to the free space. Referring to Figs. 3(b) and 3(c), two electric resonances are found to be at 2.5 GHz and 10.02 GHz, and three magnetic resonances are observed to occur at 7.94 GHz, 8.93 GHz, and 10.7 GHz, respectively. Although the fundamental electric resonance below the plasma frequency is not manifested pronouncedly in the magnitude of transmission coefficients S_{21}, it can be evidently identified from the transmission phase of S_{21} which commonly varies drastically.[32] Three negative permeability bands and two negative permittivity bands are expected, which is the critical factor of the two engineered LH bands. In the frequency ranges of 7.94 GHz–8.34 GHz and 8.93 GHz–12 GHz, the real parts of effective μ_{eff} are negative, whereas the real parts of effective ε_{eff} are negative in ranges of 2.5 GHz–8.34 GHz and 10.02 GHz–11.25 GHz, respectively. Therefore, two LH bands where negative ε_{eff} and μ_{eff} overlapped are 7.94 GHz–8.34 GHz and 10.02 GHz–10.25 GHz coincide well with the two negative refractive index bands shown in Fig. 3(d). Beyond these two bands, there is also a right-handed (RH) band (8.34 GHz–8.93 GHz) continuing in the fundamental LH band, implying that the designed LHM is balanced[5] and the composite passband comprises not only a lower LH contribution but also a higher RH band. The balanced condition is achieved through an equality of the magnetic and electric plasma frequencies.

The fundamental magnetic resonance with the real part of μ_{eff} ranging from 4 down to -15 is much stronger than the remaining two magnetic ones. Likewise, the strength of negative electric response at fundamental resonance is a few orders of magnitude larger than that at second electric resonance. It is worth while to mention that the band of negative permeability sustained to a higher frequency range beyond the observed upper terminal. This physical phenomenon can be understood from the cascaded multi-resonances of permeability of specific C-SRRs. Although the cell dimensions go beyond the limit of effective medium and the LHM does not show any evidence for LH behaviour beyond the observed frequencies, the weak magnetic resonances exist indeed in higher bands. Consequently, we concentrate on the study of these three magnetic resonances for an LHM design.

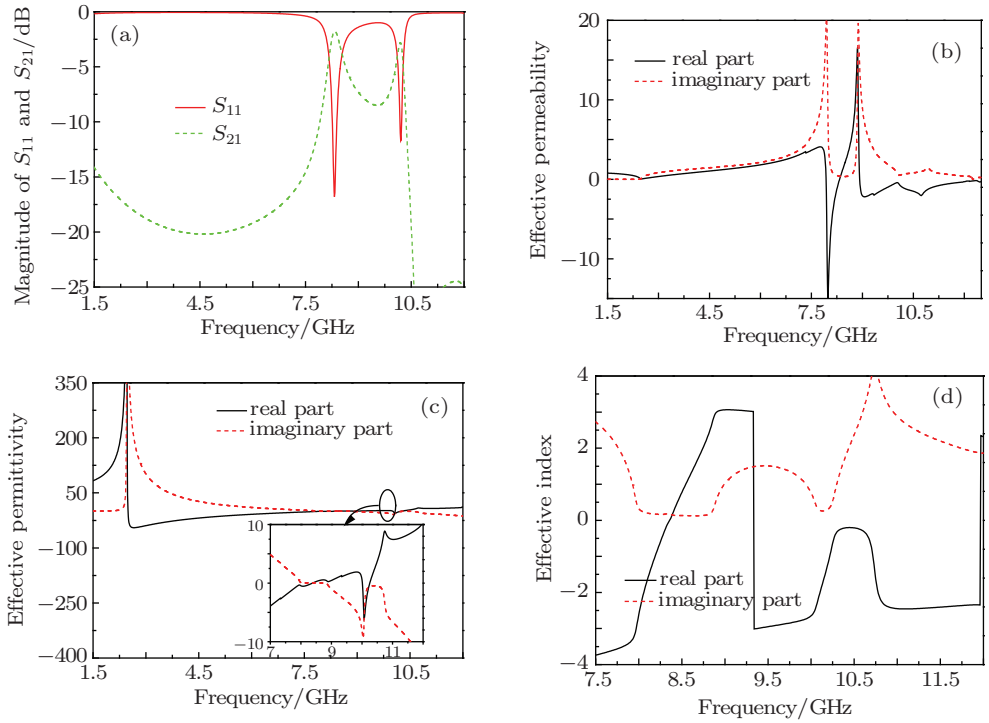


Fig. 3. (colour online) Simulated S parameters as well as the effective constitutive EM parameters: (a) magnitudes of S_{11} and S_{21}, (b) effective permeability, (c) effective permittivity, and (d) effective refractive index.

A further inspection from Fig. 3 also reveals that the third resonance in real part of permeability is accompanied by anti-resonant behaviour in the imaginary part of permeability. Moreover, the resonant permeability in the vicinity of fundamental resonance and third magnetic resonance is also accompanied by anti-resonant permittivity. These artifacts are due to the finite dimensions of the periodic structure[37] which is relative to the inherent inhomogeneity of LHM. In addition, the imaginary parts of $\mu_{\rm eff}$ and $\varepsilon_{\rm eff}$ are routinely opposite in sign among several resonance intervals, which have been seen in most of metamaterial papers. In the opinion of the authors, this is physically reasonable because both electric and magnetic fields act simultaneously on the material which is different from the case when either magnetic or electric field is assigned to the body requiring simultaneous positive values of $\mathrm{Im}(\mu_{\rm eff})$ and $\mathrm{Im}(\varepsilon_{\rm eff})$ argued in previous work.[37] The imaginary part of $\mu_{\rm eff}$ ($\varepsilon_{\rm eff}$) indicative of a magnetic (electric) gain represents the conversion of the energy from an electric (magnetic) dipole to a magnetic (electric) one and *vice versa*. However, this conversion does not obey the physical law that the total dissipated energy is always positive for passive medium under an $\mathrm{e}^{-\mathrm{j}\omega t}$ time convention.

Note that the mechanism of the stopband between two passbands seemingly resembles the MB LHM in Ref. [2], but in essence different from it. In latter case, the $\mu_{\rm eff}$ is negative only in the frequency range of magnetic resonance while the $\varepsilon_{\rm eff}$ is negative over all the considered frequency range. As a consequence, a stopband is found outside the LH band where the $\varepsilon_{\rm eff}$ is negative and $\mu_{\rm eff}$ is positive. As to the LHM proposed in this paper, the stopband is engineered because of the negative electric response in a broad range of negative magnetic response.

For demonstration and no loss of generality, an MB LHM example is designed, fabricated, and measured. In fabrication, the substrate and structure parameters are kept the same as those used in simulation, and the bulk LHM illustrated in Fig. 2 is composed of 20×2×1 of the original LHM unit cells. The substrates on which the tree-shaped metals are positioned are stacked alternatively, then put together by adhesives and finally reinforced by a hot press. The sample is placed into a standard waveguide BJ100. Scattering parameters of the fabricated MB LHM are recorded by the Agilent network analyzer HP8720ES. Figure 4 illustrates the picture of the fabricated MB LHM together with the measured frequency spectra in a narrow frequency range.

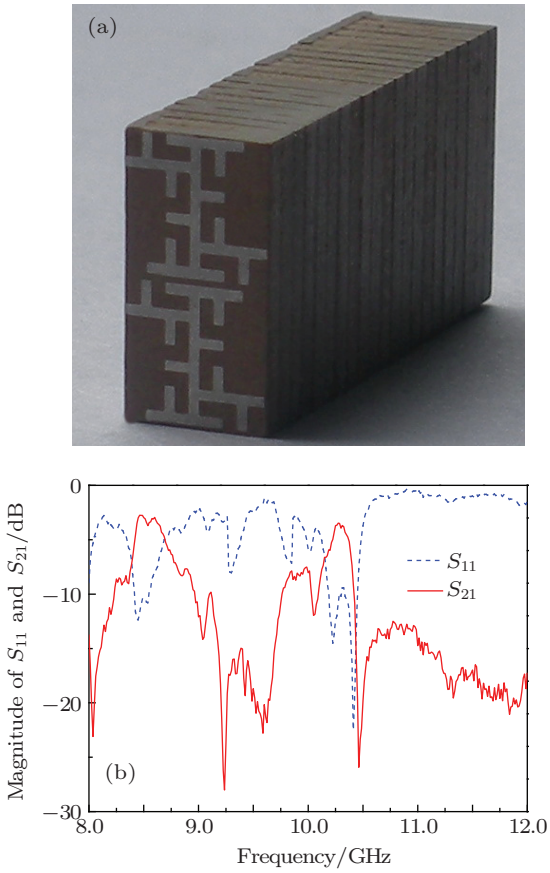


Fig. 4. (colour online) (a) Picture of the fabricated sample and (b) the measured scattering parameters.

Consulting the figure, very reasonable agreement can be observed between Figs. 3(a) and 4(b), which confirms the design. There are also two obvious transmission peaks centred at 8.5 GHz and 10.3 GHz, respectively in the measurement case. The transmission rates are on the orders of 72.9% and 67%, respectively. Slightly larger loss in the measurement relative to simulation is partially induced by the adhesives we used for robustness in the experiment and partially by the absorption of the dielectric boards[38] due to the non-ideal available substrate parameters in practice. Notice that the Ohmic loss is also not negligible.[39] The lossy effect increases as frequency becomes higher. To identify the resulting LH and RH bands, the effective μ_{eff} and ε_{eff} retrieved from measured scattering parameters are depicted in Fig. 5. Referring to the figure, we conclude that the real part of μ_{eff} takes negative values in 8.12 GHz–8.56 GHz and 8.99 GHz–12 GHz, respectively, whereas the real part of ε_{eff} is negative in 8.12 GHz–8.56 GHz and 10.1 GHz–10.47 GHz. Therefore, two LH bands with simultaneous negative ε_{eff} and μ_{eff} are 8.12 GHz–8.56 GHz and 10.1 GHz–10.47 GHz, respectively. The most exciting behaviour is that the LHM with a composite fundamental passband is still balanced.

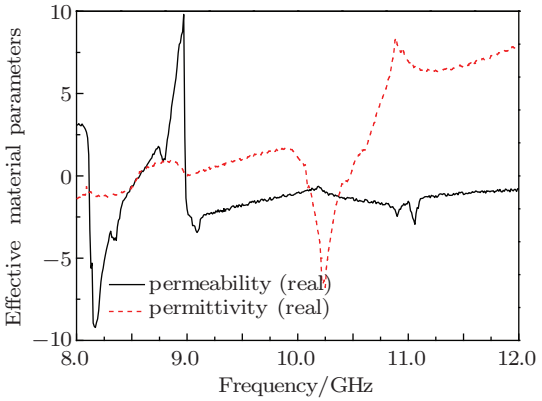


Fig. 5. (colour online) Real parts of the effective permeability and effective permittivity retrieved from measured scattering parameters.

To further verify the LH characteristic of the proposed LHM slab in higher band, the intrinsic effective propagation constant β which is a function of frequency and contains important information about the extracted EMPs of a periodic medium, is obtained by using the eigenmode analysis in Ansoft HFSS. The eigenmode approach is used to solve the nature resonance of the structure, which does not require any excitation. To mimic the simulation setup shown in Fig. 2 and also to yield β in the propagation direction, two walls along the x axis are modeled as being a perfect magnetic conductor (PMC) and those along y axis and z axis are assigned as master/slave in HFSS. It is worth while to mention that there is still an unavoidable slight discrepancy between this setup and that shown in Fig. 2, namely infinite periodic cells along z direction in the former case while only one cell in the latter case. Figure 6 shows the dispersion diagram of the proposed tree-shaped LHM slab in the ΓZ part of the Brillouin zone. From this figure, one can observe that the material behaves as an LH medium in higher band (RH medium in lower band) since the dispersion has negative gradient through the Brillouin zone from 9.5 GHz to 10.3 GHz. The upper edge of LH band coincides well with 10.25 GHz that is predicted in Fig. 3, whereas the lower edge is significantly lower than that in Fig. 3. Despite these, the RH bands are in good agreement in both cases. The lower edge of upper LH band (wider LH band) and the lower composite LH and RH bands that have disappeared are

mainly attributed to the coupling between adjacent cells in propagation direction, which has been well established in Ref. [40]. This is especially for the slightly large element dimensions of the LHM proposed in this paper which is far from the criterion that the wavelength is 30 times larger than the length of unit cell.

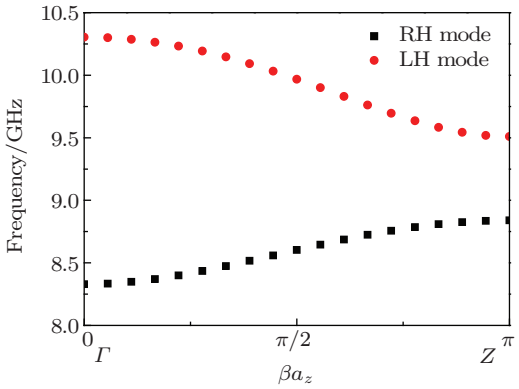


Fig. 6. (colour online) Dispersion diagram of the proposed tree-shaped LHM slab.

3. Field distribution analysis

To illustrate the underlying multi-resonant mechanism from a physical insight, the surface current and electric field distributions of the MB LHM in the y–z plane at the magnetic and electric resonances are shown in Figs. 7 and 8, respectively. At the fundamental magnetic resonance in Fig. 7(a), C-SRR$_1$ and C-SRR$_6$ resonate mutually according to the strong current density (mutual coupling illustrated above) along horizontal metallic strips in the up-and-down region. The enhanced localized circular surface currents in conjunct area of C-SRR$_1$ and C-SRR$_6$ with biggest zig–zag current loop formed (marked with blue arrows) are responsible for the strong magnetic response in the lowest band. This statement finds strong support from the current distribution shown in Fig. 7(b) at the second magnetic resonance frequency 8.93 GHz, where C-SRR$_3$ and C-SRR$_5$ resonate mutually and the current density is enhanced in the conjunct area of them not so strongly and the circumscribed rectangle loop is not so big in comparison with the former case, thereby accounting for the weak magnetic resonance. Due to the interplay of these C-SRRs, the resonant particles also induce a strong surface current in other regions, e.g., the resonance of C-SRR$_1$ and C-SRR$_6$ yields a comparable current density in regions from C-SRR$_2$ to C-SRR$_5$. At 10.7 GHz, C-SRR$_1$ or C-SRR$_6$ resonates individually and the strength is on the order of that at the second resonance. The smallest current loop is responsible for the third magnetic resonance. In the same manner, the resonant particles also result in strong currents in other nonresonant C-SRRs.

As discussed above, the upper broadband negative magnetic response is engineered because multi-magnetic resonant modes are formed and cascaded. In other words, a chain of sub-circuits with different capacitances and inductances are shaped into different C-SRRs. For demonstration, extensive simulations of current distributions are performed from the third magnetic resonances up to the terminal frequency of negative permeability. An enhanced localized circular current always dominates in some specific C-SRR within the band but contrarily it does not show any evidence for this phenomenon outside the band, indicating that the occurrence of various circular currents (potential magnetic resonances) is the key factor to maintain the broadband negative magnetic response. The appearance of enhanced circular currents takes turns among these C-SRRs in an underlying law. One thing is clear that, say, different C-SRRs resonate at different magnetic resonant frequencies with different magnitudes which can be adopted in the design of controllable magnetic metamaterials.

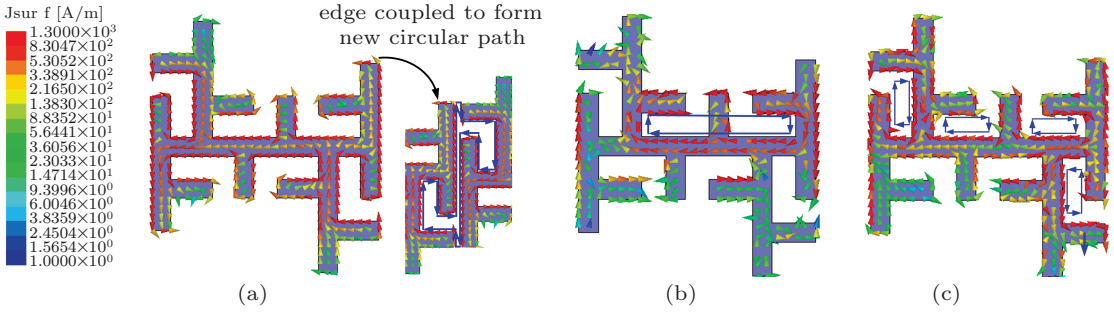


Fig. 7. (colour online) Surface current distributions in y–z plane at (a) 7.94 GHz, (b) 8.93 GHz, and (c) 10.7 GHz.

In summary, at least three current loops with different magnitudes are engineered, corresponding to three independent magnetic dipoles. The inductive magnetic fields at each resonance are large and antiparallel with respect to the excited ones, which is responsible for three negative permeability bands.

From the fields distribution shown in Fig. 8(a), very obvious uniform electric fields pointing from one end to the other in the up-and-down region resemble an electric dipole, corresponding to the resonant behaviour of a cut wire at 2.5 GHz. The dipole moment is weakened gradually from 2.5 GHz to 8.37 GHz (the fundamental electric plasma frequency $\omega_{\rm ep}^{(1)}$) because of the side opposite electric field. Despite this, the predominant dipole moment still holds and thus negative $\varepsilon_{\rm eff}$ can be expected to be below $\omega_{\rm ep}^{(1)}$. Referring to Fig. 8(b), the asymmetric ELC resonator resonates at 10.02 GHz and plays a predominant role. The uniform electric field originates accordingly from the bottom arm to the top one at both sides, resembling the behaviour of conventional ELC resonator.[8] In both cases, the inductive uniform electric fields are opposite to in sign, but larger in magnitude than the incident electric fields, thereby giving rise to the negative permittivity in the vicinity of two resonances. Therefore, the strong electric dipole moment accounts for the negative electric response.

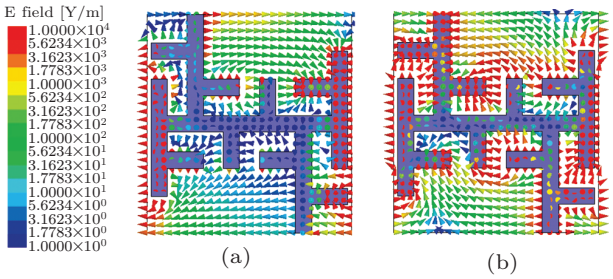


Fig. 8. (colour online) Electric field distributions in y–z plane at (a) 2.5 GHz and (b) 10.02 GHz.

4. Circuit model analysis

In this section, we present a circuit analysis to show how the tree-shaped LHM produces negative $\mu_{\rm eff}$ and $\varepsilon_{\rm eff}$ over multi-frequency bands and derive analytical formulas to provide qualitative prediction and controllability[41] over these resonances. This can be carried out provided that the LHM cell is a small fraction of the free-space wavelength at the operating frequency. Figure 9 shows the proposed equivalent circuit model of a typical unit cell. Multi-sub-circuits are cascaded with different values of capacitance (C) and inductance (L), representing multi-resonant modes. $L_{\rm e1}$ and $C_{\rm e1}$ indicate the oscillations of linear current along the central pole and gap, accounting for the fundamental electric resonance, whereas $L_{\rm e2}$ and $C_{\rm e2}$ are related to the electric resonance of the ELC resonator. The three magnetic resonances are modeled orderly by $L_{\rm m1}$ and $C_{\rm m1}$, $L_{\rm m2}$ and $C_{\rm m2}$, and $L_{\rm m3}$ and $C_{\rm m3}$.

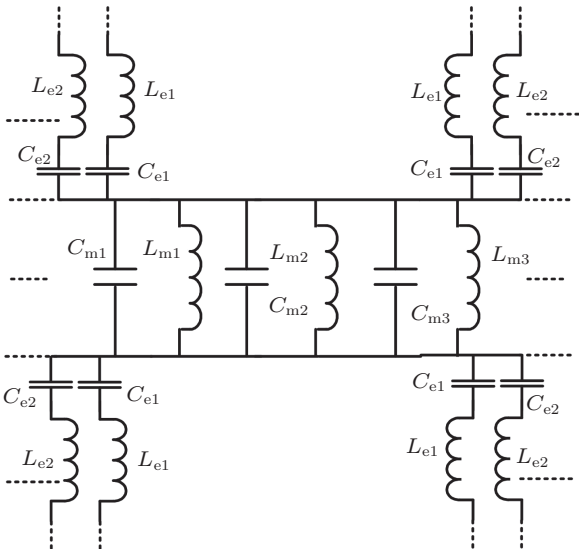


Fig. 9. Equivalent circuit model of the proposed LHM at magnetic and electric resonances.

The capacitance $C_{\rm e1}$ formed between horizontal metallic strips in the up-and-down region of two adjacent LHM cells is related to periodicity a_y and can be approximated by

$$C_{\rm e1} = A\frac{\varepsilon_0\varepsilon_{\rm r}' l}{\pi}\ln\left(\frac{2w}{a_y - h}\right), \tag{4}$$

where $\varepsilon_{\rm r}'$ is the effective permittivity with $1 < \varepsilon_{\rm r}' < 9.6$, and A is the constant used to compensate the complex interplay of the horizontal C-SRRs. $L_{\rm e1}$ models the inductance of the central pole, including the self-inductance $L_{\rm es}$ and mutual inductance $L_{\rm em}$ due to the small spacing of adjacent cells along the x axis. Value of $L_{\rm es}$ is evaluated as[42]

$$L_{\rm es} \approx \frac{\mu_0 h}{\pi}\ln\left(\frac{6.6h}{w}\right), \tag{5}$$

while $L_{\rm em}$ is approximated by

$$L_{\rm em} = \frac{\mu_0 h}{2\pi}\left(\ln\frac{2h}{a_x} - 1\right). \tag{6}$$

Then the fundamental electric resonance $\omega_{\rm e0}^{(1)}$ is directly predicted as

$$\omega_{\rm e0}^{(1)} = 1/\sqrt{(L_{\rm es}+L_{\rm em})C_{\rm e1}} = 1\Big/\sqrt{\frac{\mu_0 A}{2\pi}\left(\frac{5b}{9}+w\right)\left(\frac{2b}{9}+w\right)} \times 1\Big/\sqrt{\left\{\ln\left[\frac{87.12\times(5b/9+w)^3}{w^2 a_x}\right]-1\right\}\frac{\varepsilon_0\varepsilon'_{\rm r}}{\pi}\ln\left(\frac{2w}{a_y-w-5b/9}\right)}. \quad (7)$$

The electric plasma frequency $\omega_{\rm ep}^{(1)}$ can be formulated in a first approximation by Pendry *et al.*'s formula[30]

$$\omega_{\rm ep}^{(1)} = \frac{2\pi c_0^2}{a^2\ln(a/r)}, \quad (8)$$

where a and r are the periodicity of the wire array and wire radius, respectively. Although the cross section of the central pole considered here is rectangle whereas it was circular in Pendry *et al.*'s model, the plasma frequency takes a similar function which can be employed as a rough guide for balanced LHM design. The frequency for electric resonance of asymmetric ELC resonator, $\omega_{\rm e0}^{(2)}$, is also a function of $L_{\rm e2}$ and $C_{\rm e2}$ and takes a similar formulation to Eq. (7). In the present design, values of $L_{\rm e2}$ and $C_{\rm e2}$ each are a continuous function of not only geometrical parameters of ELC resonator (i.e., b, $g_{\rm v}$, $g_{\rm h}$, and w) but also lattice constants a_x and a_y through the front-and-back broadside coupling and up-and-down edged coupling.

As to the case of fundamental magnetic resonance, the capacitance $C_{\rm m1}$ should contain two contributions, say, the coupling effect $C'_{\rm m1}$ between front-and-back adjacent cells and gap capacitance $C''_{\rm m1}$. In both cases, they are approximated by parallel-plate capacitance formula as

$$\begin{cases} C_{\rm m1} = C'_{\rm m1} + C''_{\rm m1}/2, \\ C'_{\rm m1} = \varepsilon_0\varepsilon'_{\rm r}\dfrac{wl_1}{a_x}, \\ C''_{\rm m1} = B\varepsilon_0\varepsilon'_{\rm r}\dfrac{wt}{a_y-5b/9-w}, \end{cases} \quad (9)$$

where correctional coefficient B is used to include the strong EM brink effect, and l_1 is the total perimeter of the zig–zag loop and given as

$$l_1 = 4b/9 + 2a_y + 2g_{\rm h}. \quad (10)$$

It is well established that the self-inductance per unit length of a circular loop with strip width w and radius r can be approximated according to loop antenna theory[43] as

$$L_m = \mu_0 r\left[\log\frac{32r}{w}-2\right]. \quad (11)$$

This corresponding theory still holds for current zig–zag loop, however, an equivalent circular loop with transformed r should be established first. Therefore, the per-unit-length inductance of the loop is formulated by amending Eq. (11) through a correctional factor C

$$L_{\rm m1} = C\mu_0\frac{l_1}{2\pi}\left[\log\frac{16l_1}{\pi w}-2\right]. \quad (12)$$

Thus $\omega_{\rm m0}^{(1)}$ is directly formulated as

$$\omega_{\rm m0}^{(1)} = \frac{1}{\sqrt{L_{\rm m1}C_{\rm m1}}} = 1\Big/\sqrt{\frac{C\varepsilon_0\varepsilon'_{\rm r}\mu_0 wl_1}{2\pi}\left[\frac{l_1}{a_x}+\frac{Bt}{2(a_y-5b/9-w)}\right]\left[\log\frac{16l_1}{\pi w}-2\right]}. \quad (13)$$

In the same manner, we obtain the following formulas to estimate the second and third magnetic resonant frequencies:

$$\omega_{\rm m0}^{(2)} = \frac{1}{\sqrt{L_{\rm m2}C_{\rm m2}}} = 1\Big/\sqrt{\frac{5C\varepsilon_0\varepsilon'_{\rm r}\mu_0 wb}{9\pi}\left(\frac{10b}{9a_x}+\frac{Bt}{2g_{\rm v}}\right)\left[\log\frac{160b}{9\pi w}-2\right]}, \quad (14)$$

$$\omega_{\rm m0}^{(3)} = \frac{1}{\sqrt{L_{\rm m3}C_{\rm m3}}} = 1\Big/\sqrt{\frac{3C\varepsilon_0\varepsilon'_{\rm r}\mu_0 wb}{9\pi}\left(\frac{6b}{9a_x}+\frac{Bt}{g_{\rm h}}D_{gap}\right)\left[\log\frac{96b}{9\pi w}-2\right]}, \quad (15)$$

where $D_{\rm gap}$ models the fringe capacitive effect of horizontal strips and is a function of gap. Given these three magnetic resonances, the corresponding three magnetic plasma frequencies $\omega_{\rm mp}^{(1)}$, $\omega_{\rm mp}^{(2)}$, and $\omega_{\rm mp}^{(3)}$ can be straightly obtained according to Eq. (3). According to the simulation results of the LHM slab, the balanced condition of a zero-gap LHM is

$$\omega_{\rm mp}^{(1)} = \omega_{\rm ep}^{(1)}. \quad (16)$$

5. Controllability over multi-resonances

Now that we have derived some basic formulations to quantitatively design these resonant frequencies, we come to see how geometrical parameters physically influence the LH behaviour. This study would proof-test the rationality of former derivations and affords us a complete understanding of the working mechanism. Figures 10 and 11 show the effect of lattice constants a_x and a_y on the LH transmission behaviour, respectively. Referring to Fig. 10, both electric and magnetic resonant frequencies increase with the value of a_x increasing, e.g, when a_x increases from 1 mm to 2 mm in steps of 0.5 mm, $\omega_{\mathrm{m0}}^{(1)}$, $\omega_{\mathrm{m0}}^{(2)}$, and $\omega_{\mathrm{m0}}^{(3)}$ shift upwards gradually from 7.94 GHz, 8.93 GHz, and 10.7 GHz to 10.85 GHz, 11.8 GHz, and 13.54 GHz, respectively, whereas $\omega_{\mathrm{e0}}^{(1)}$ and $\omega_{\mathrm{e0}}^{(2)}$ increase from 2.5 GHz and 10.02 GHz to 3.9 GHz and 12.87 GHz, respectively. We also remark that $\omega_{\mathrm{ep}}^{(1)}$ shifts from 8.34 GHz to 9.88 GHz. The variational bands of negative permittivity and permeability result in the absence of LH behaviour. These results are consistent well with aforementioned discussion and find strong support from Eqs. (7), (8), and (13)–(15). Given the sensitivity of a_x, it is advisable to choose a_x as the height of the substrate to avoid any tolerance in fabrication and measurement.

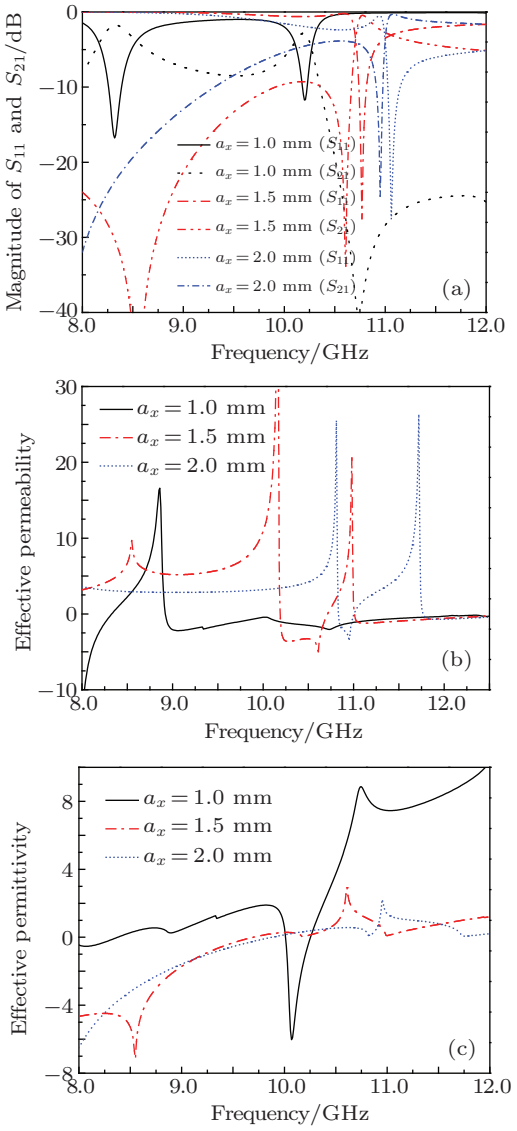


Fig. 10. (colour online) Frequency-dependent simulated S parameters and the effective constitutive EM parameters (real part) versus a_x: (a) magnitudes of S_{11} and S_{21}, (b) effective permeability, and (c) effective permittivity.

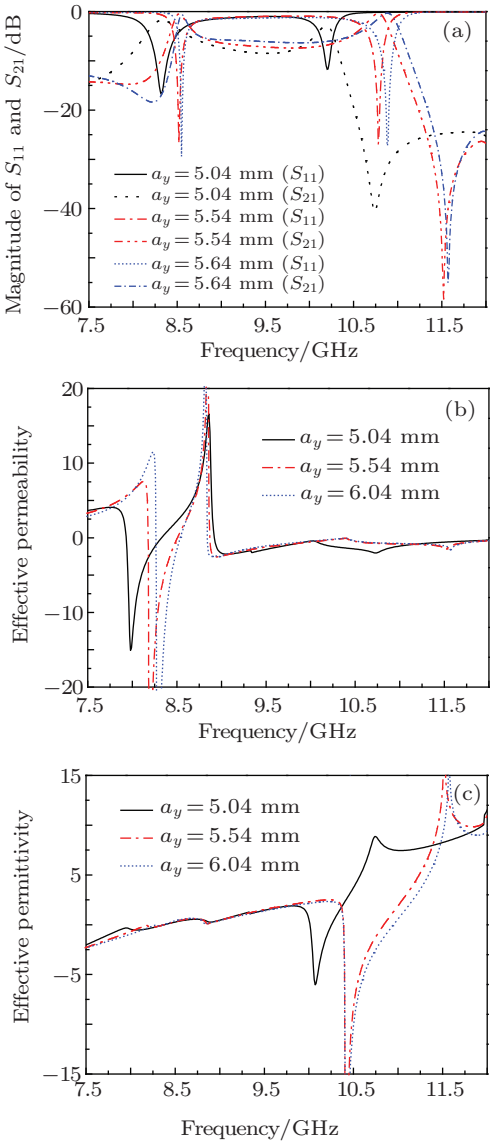


Fig. 11. (colour online) Frequency-dependent simulated S parameters and the effective constitutive EM parameters versus a_y: (a) magnitudes of S_{11} and S_{21}, (b) effective permeability, and (c) effective permittivity.

Consulting Fig. 11, two obvious LH passbands always exist no matter how a_y changes from 5.04 mm to 6.04 mm. The variation of a_y equals the change of the gap between neighbouring cells in essence. The fundamental LH band shifts upward slightly with the value of a_y increasing while the second LH band increases at a larger speed. The increasing rates of $\omega_{\rm m0}^{(1)}$ and $\omega_{\rm e0}^{(2)}$ are exactly or almost the same as those of the first and second LH band, respectively, thereby accounting for the macroscopic change of S-parameter. The variations of $\omega_{\rm m0}^{(1)}$ and $\omega_{\rm e0}^{(2)}$ saturate because $C_{\rm m1}$ and $C_{\rm e2}$ are partially determined by the gap and reduce with a_y increasing as indicated in Eq. (9). When a_y increases to such an extent that the effect is negligible, the other constituent part dominates the $C_{\rm m1}$ and $C_{\rm e2}$, leading to the stabilization of two LH bands. A further inspection also indicates that $\omega_{\rm e0}^{(1)}$ and $\omega_{\rm m0}^{(3)}$ shift from 2.5 GHz and 10.7 GHz to 3.61 GHz and 11.57 GHz, respectively. The saturation of variation of $\omega_{\rm m0}^{(3)}$ is also observed and the mechanism is the same as that of $\omega_{\rm m0}^{(1)}$, whereas $\omega_{\rm e0}^{(1)}$ shifts continuously as indicated in Eqs. (4) and (7). Despite these, an exciting characteristic of the LHM slab should be that $\omega_{\rm m0}^{(2)}$ is almost fixed around 9 GHz as shown in Eq. (14).

To further validate the established theory for the tree-shaped LHM, we examine the roles of geometrical parameters $g_{\rm v}$ and $g_{\rm h}$ by performing simulations for the three individual cases: the first case, uniform case, where $g_{\rm v} = g_{\rm h} = 0.48$ mm, the second case where $g_{\rm v} = 0.24$ and $g_{\rm h} = 0.48$ mm, and the last case where $g_{\rm v}$=$g_{\rm h}$ = 0.24 mm. In Fig. 12 we compare the simulated S-parameters with constitutive EM parameters. A macroscopic inspection implies that $g_{\rm v}$ plays an important role in affecting $\omega_{\rm m0}^{(2)}$ and $\omega_{\rm e0}^{(2)}$, and so does $g_{\rm h}$ in influencing $\omega_{\rm m0}^{(3)}$ and $\omega_{\rm e0}^{(2)}$. Therefore, the upward shiftings of $\omega_{\rm e0}^{(2)}$ with $g_{\rm v}$ and $g_{\rm h}$ increasing are responsible for the sharp variation of upper LH band, whereas the slight discrepancy of $\omega_{\rm m0}^{(1)}$ accounts for the almost fixed fundamental LH band. It is worth while to mention that $\omega_{\rm e0}^{(1)}$ always retains around 2.5 GHz in both cases as shown in Eq. (7). For completeness of content, we also investigate the effects of b and w. However, their results are not provided for brevity. Here, we review and draw directly the conclusion, i.e., all the magnetic and electric resonances shift downwards as b increases, while they increase with w increasing. To sum up, the results shown in Figs. 10–12 are in good agreement with those shown in circuit model analysis, unambiguously providing a useful guideline for independent control over these multi-resonant frequencies and in turn facilitating controllable LH behaviour.

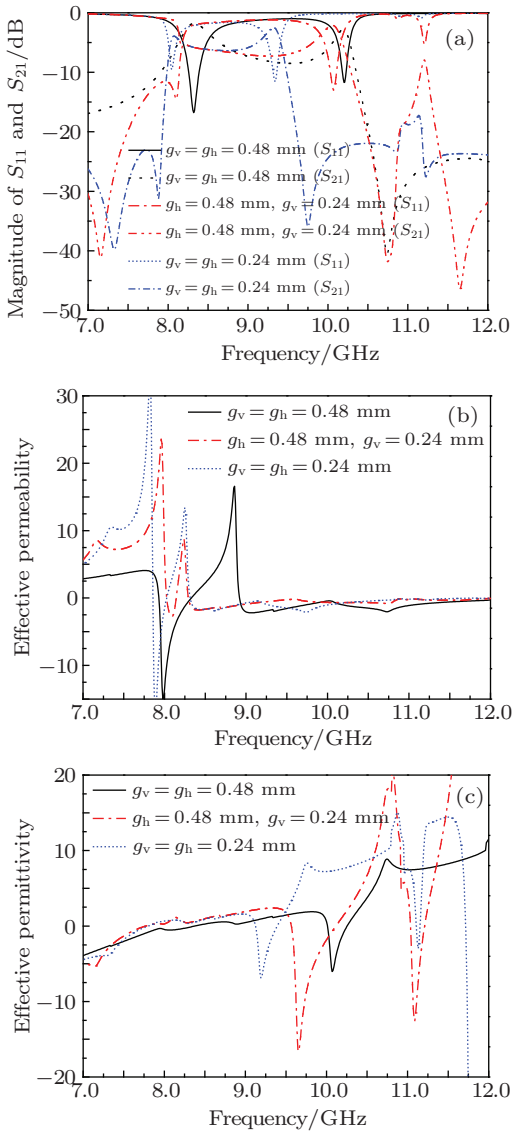


Fig. 12. (colour online) Frequency-dependent simulated S parameters and the effective constitutive EM parameters of the MB LHM versus split width: (a) magnitudes of S_{11} and S_{21}, (b) effective permeability, and (c) effective permittivity.

6. Conclusion

In this paper, both simulations and measurement clearly show the viability of using tree-shaped fractals to build dual-band LHM. The multi-resonant mechanism is identified and validated. The method of realizing MB LHM has reference values in designing new types of planar MB LHMs. Moreover, the broad higher magnetic resonance can also be designed to have its negative permeability overlapped with the negative permittivity of other electric resonators to build wideband LHMs.

References

[1] Shelby R A, Smith D R and Schultz S 2001 *Science* **292** 77

[2] Chen H S, Ran L X, Huangfu J T, Zhang X M, Chen K S, Grzegorczyk T M and Kong J A 2004 *J. Appl. Phys.* **96** 5338

[3] Tretyakov S A 1998 *J. Electrom. Waves Appl.* **12** 821

[4] Huangfu J T, Ran L X, Chen H S, Zhang X M, Chen K S, Grzegorczyk T M and Kong J A 2004 *Appl. Phys. Lett.* **84** 1537

[5] Lheurette É, Houzet G, Carbonell J, Zhang F L, Vanbésien O and Lippens D 2008 *IEEE Trans. Antennas Propag.* **56** 3462

[6] Bulu I, Caglayan H and Ozbay E 2005 *Opt. Express* **13** 10238

[7] Zhou J, Koschny T, Zhang L, Tuttle G and Soukoulis C M 2006 *Appl. Phys. Lett.* **88** 221103

[8] Zhou J, Zhang L, Tuttle G, Koschny T and Soukoulis C M 2006 *Phys. Rev.* B **73** 041101(R)

[9] Chen C H, Qu S B, Wang J F, Ma H, Wang X H and Xu Z 2011 *Chin. Phys.* B **20** 034101

[10] Yao Y and Zhao X P 2007 *J. Appl. Phys.* **101** 124904

[11] Kafesaki M, Tsiapa I, Katsarakis N, Koschny T, Soukoulis C M and Economou E N 2007 *Phys. Rev.* B **75** 235114

[12] Liu Y H, Luo C R and Zhao X P 2007 *Acta Phys. Sin.* **56** 5883 (in Chinese)

[13] Liu R, Degiron A, Mock J J and Smith D R 2007 *Appl. Phys. Lett.* **90** 263504

[14] Wang J F, Qu S B, Yang Y M, Ma H, Wu X and Xu Z 2009 *Appl. Phys. Lett.* **95** 014105

[15] Zhu W R, Zhao X P and Ji N 2007 *Appl. Phys. Lett.* **90** 011911

[16] Huang Y J, Wen G J, Yang Y J and Xie K 2012 *Appl. Phys.* A **106** 79

[17] Guo Y and Xu R 2006 *Progress in Electromagnetics Research* **66** 239

[18] Kwon D H, Werner D H, Kildishev A V and Shalaev V M 2007 *Opt. Express* **15** 1647

[19] He X J, Wang Y, Mei J S, Gui T L and Yin J H 2012 *Chin. Phys.* B **21** 044101

[20] Xu H X, Wang G M, Liu Q, Wang J F and Gong J Q 2012 *Appl. Phys.* A **107** 261

[21] Gu C, Qu S B, Pei Z B, Xu Z, Liu J and Gu W 2011 *Chin. Phys.* B **20** 017801

[22] Xu H X, Wang G M and Liang J G 2011 *Radio Sci.* **46** RS5008

[23] Xu H X, Wang G M and Wang X 2011 *Electron. Lett.* **47** 1081

[24] Wen W, Zhou L, Hou B, Chan C T and Sheng P 2005 *Phys. Rev.* B **72** 153406

[25] Hao J M, Zhou L and Chan C T 2007 *Appl. Phys.* A **87** 281

[26] Zhao G Z, Tian Y, Sun H Q, Zhang C L and Yang G Z 2006 *Chin. Phys. Lett.* **23** 1456

[27] Du Q J, Liu J S, Yang H W and Yi X N 2011 *Appl. Opt.* **50** 4798

[28] Soukoulis C M, Linden S and Wegener M 2007 *Science* **315** 47

[29] Xu L and Michael Y W C 1999 *Microwave Opt. Technol. Lett.* **23** 242

[30] Pendry J B, Holden A J, Stewart W J and Youngs I 1996 *Phys. Rev. Lett.* **76** 4773

[31] Chen X D, Grzegorczyk T M, Wu B I, Pacheco J and Kong J A 2004 *Phys. Rev.* E **70** 016608

[32] Smith D R, Vier D C, Koschny Th and Soukoulis C M 2005 *Phys. Rev.* E **71** 036617

[33] Urbani F 2010 *IEEE Antennas Wireless Propag. Lett.* **9** 720

[34] Simovski C R 2011 *J. Opt.* **13** 013001

[35] Alu A 2011 *Phys. Rev.* B **83** 081102(R)

[36] Smith D R 2010 *Phys. Rev.* E **81** 036605

[37] Koschny T, Markoš P, Economou E N, Smith D R, Vier D C and Soukoulis C M 2005 *Phys. Rev.* B **71** 245105

[38] Markoš P, Rousochatzakis I and Soukoulis C M 2002 *Phys. Rev.* E **66** 045601(R)

[39] Wang J F, Qu S B, Xu Z, Zhang J Q, Ma H, Yang Y M and Gu C 2009 *Chin. Phys. Lett.* **26** 084103

[40] Zhou J F, Koschny T, Kafesaki M and Soukoulis C M 2008 *Photonics and Nanostructures–Fundamentals and Applications* **6** 96

[41] Wang J F, Qu S B, Xu Z, Ma H, Yang Y M and Gu C 2008 *IEEE Trans. Antennas Propag.* **56** 2018

[42] Bahl I and Bhartia P 2003 *Microwave Solid State Circuit Design* (New Jersey: John Wiley & Sons) pp. 58–60

[43] Simovski C R, Belov P A and He S L 2003 *IEEE Trans. Antennas Propag.* **51** 2582